Microstructure Development during High-Velocity Deformation

P.J. FERREIRA, J.B. VANDER SANDE, M. AMARAL FORTES, and A. KYROLAINEN

An austenitic stainless steel was deformed at high (10^3 s^{-1}) strain rates at two levels of strain by electromagnetic forces. Transmission electron microscopy (TEM) studies, X-ray diffraction analysis, and superconducting quantum-interference device (SQUID) measurements show that high strain rates induce the formation of stacking faults and twin structures, enhance the tendency for ε-martensite formation, and suppress the amount of α'-martensite. The increased presence of stacking faults and twin structures at high strain rates can be explained by an easy nucleation of partial dislocations at high strain rates and a superior aptitude for partial dislocations to react to high strain rates due to their jump frequency. The suppression of α'-martensite can be explained by the adiabatic heating produced during electromagnetic forming.

I. INTRODUCTION

HIGH-VELOCITY deformation processes are becoming increasingly important in a significant number of technological areas and related industries. In the automotive industry, an understanding of the mechanisms occurring during high-velocity vehicle impacts is crucial to the development of materials with higher safety records. In the space industry and related spacecraft, predicting the behavior of materials in components subjected to high-velocity impact by space debris is essential to successful space exploration. Finally, in the general area of forming, improving the formability of metals can contribute significantly by helping to solve problems arising from materials with low forming limits, geometries involving high angles, and high springbacks. In high-velocity processes, all of the deformation may occur on the order of microseconds, with strain rates ranging from approximately 10^2 s^{-1} for automobile collisions to about 10^3 s^{-1} during the impact of space debris, as well as during electrohydraulic and electromagnetic forming. This regime of strain rates, in conjunction with controlled parameters such as peak pressure, peak duration, maximum strain, and predeformation, may produce unique structural and property characteristics.

It has been shown through past studies that materials deformed at high velocities exhibit extremely high ductility (100 pct elongation was observed without failure in iron, copper, and aluminum sheets)[1,2] as well as significant strain-rate sensitivity.[3] At the microstructural level, high strain rates induce a high density of dislocations,[4] large vacancy concentrations,[5] and a higher tendency for deformation twinning to substitute for slip.[6] The amount of twinning produced is a function of the peak pressure, peak duration, and stacking-fault energy (SFE) of the material.[5] In low-SFE materials,

for which we assume SFE $<$ 60 mJ/m^2, a significant number of planar defects, such as stacking faults and twins, occur at considerably lower peak pressures ($P = 1$ GPa) and with short peak durations (1 μs).[7] On the other hand, for the same level of pressures and time intervals, dislocation cell structures develop in high-SFE materials (SFE $>$ 60 mJ/m^2).[7,8] However, at higher critical pressures, high-SFE materials will eventually twin under high-velocity deformation.

One class of materials strongly affected by deformation at high strain rates is the group of austenitic stainless steels. When deformed at high velocities, the microstructure of low-SFE austenitic stainless steels exhibits large amounts of deformation twins, a significant fraction of stacking faults, ε-martensite, and, as expected, α'-martensite. The relative quantities of each phase are dependent on various factors such as strain rate, strain, peak pressure, pulse duration, crystallographic orientation, temperature, and grain size. As a consequence, by affecting the phase balance, the processing conditions can strongly influence the properties of the material.

For stainless steel compositions that allow the existence of metastable phases, in the range of temperatures selected for high-velocity deformation, modifications in phase quantity may occur. This is particularly true in low-SFE austenitic stainless steels, for which the tendency for α'-martensite formation is reduced for higher strain rates.[9,10] This behavior seems to be associated with the adiabatic heating produced during deformation at high velocities and its effects on the transformation temperature.[9,10] In addition, under similar high-strain-rate conditions, the amount of martensite produced can be altered by controlling the peak pressure and pulse duration.[11] Typically, a higher peak pressure and a longer pulse duration result in larger volume fractions of α'-martensite.

The influence of experimental parameters during high-velocity deformation on the mechanism of deformation twinning has been discussed,[5–8] although controversy still exists. In contrast, the interplay between the formation of α-martensite, ε-martensite, twins, stacking faults, and dislocation substructures and the effect caused by the application of high strain rates on the nucleation of these structures and the motion of dislocations have seen little discussion. In the present work, a type-304 austenitic stainless steel has been deformed at high velocities under an electromagnetic force. While recognizing that this method of processing may become very attractive for the rapid production of deformable pieces, we also intend to

P.J. FERREIRA, Assistant Professor, is with the Materials Science and Engineering Program, University of Texas at Austin, Austin, TX 78712. Contact e-mail: ferreira@mail.utexas.edu. J.B. VANDER SANDE, Professor, is with the Department of Materials Science and Engineering, Massachusetts Institute of Technology, Cambridge, MA 02139. M. AMARAL FORTES, Professor, is with the Department of Materials Engineering, Instituto Superior Técnico, Lisboa, Portugal. A. KYROLAINEN, Research Engineer, is with Outokumpu Stainless Oy, Tornio, Finland.

investigate the influence of high-velocity deformation on the microstructure achieved, in order to compare and correlate some of these results with experiments performed at low strain rates and various temperatures.

II. EXPERIMENTAL

A. *Material*

A stable austenitic stainless steel of commercial grade AISI 304, provided by Outokumpu Stainless Oy, Tornio, Finland, with the chemical composition given in Table I, was used in this investigation. The material was received with an ASTM grain size of 7 and approximately 8000 inclusions/cm^2, with inclusion sizes ranging from 1 to 10 μm. This material was chosen for its chemical stability, fcc crystal structure, paramagnetism, and low SFE. These properties are important for the studies performed in this work.

B. *Methods*

1. *High-Velocity Electromagnetic Forming*
Tubes of stainless steel with 50-mm radii and 1-mm thickness were subjected to radial forming by deforming the material onto a die induced by electromagnetic forces. The process of forming was accomplished by placing a coil around a copper conductor surrounding the stainless steel tube, which is gripped on both extremities, and, subsequently, generating an electrical pulse of very high current through the coil (Figure 1). The current in the coil generates a high magnetic field, which induces a current in the Cu/stainless steel system. The currents in both the coil and stainless steel travel in different directions and, thus, repel each other. In this fashion, a magnetic pressure

Table I. Chemical Composition in Weight Percent for AISI 304 Stainless Steel

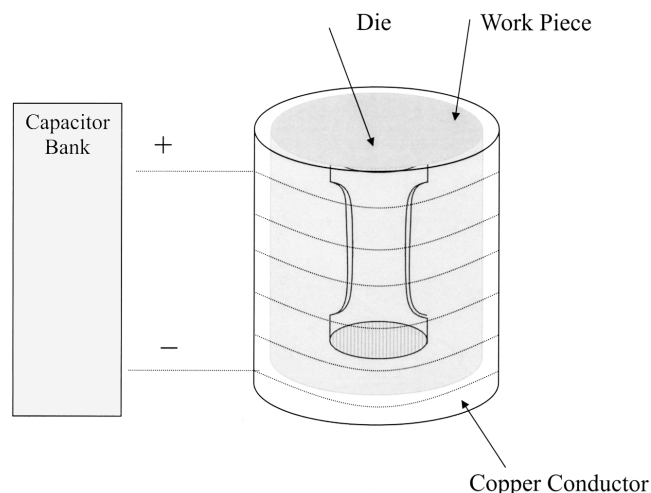| C	Cr	Ni	Mn	Si	P
0.07	18.0	8.5	1.44	0.36	0.016

Fig. 1—Schematic of the apparatus for electromagnetic forming. The currents in the workpiece and coil are in opposite directions, and as a result, they repel each other and impel the workpiece against the die. The copper conductor is used for cases where the workpiece does not have high conductivity.

was generated on the stainless steel tube, and this provided the forming energy by driving the material into the die. Kinetic energy was supplied, and, hence, the magnetic-pressure pulse enabled a high acceleration of the workpiece.

Two experiments were performed using the apparatus shown in Figure 1. In the first, the stainless steel tube was deformed in quasi-hydrostatic compression, perpendicular to the tube's longitudinal direction, at a peak pressure of 1 GPa and at an average strain rate of about 1000 s^{-1}. The transverse strain obtained was approximately 25 pct. The peak magnetic pressure (P_m) that acts on the workpiece was calculated as $P_m = B/2\mu_0$, where B is the magnetic-flux density, which is proportional to the current and the density of the windings in the solenoid, and μ_0 is the magnetic permeability of free space. The strain rate was measured by determining the change in the stainless tube radius as a function of time. The transverse strain was determined by measuring the change in dimensions of a circle which was laser-printed onto the stainless steel surface before deformation. In the second experiment, the tube was subjected to a similar test but at a lower peak pressure of 300 MPa. In the latter experiment, the transverse strain was about 5 pct. The kinetic energy was controlled by the use of copper plates with different thicknesses. In addition to these high-strain-rate tests, low-strain-rate (10^{-3} s^{-1}) uniaxial compression experiments at 25 pct strain were performed in an MTS apparatus.

2. *Characterization*
Samples with dimensions of 10 $\times$ 10 mm and 1 mm in thickness were cut along the longitudinal direction of the tubes. Therefore, the sample dimensions of 10 $\times$ 10 mm were laying perpendicular to the radial direction of the stainless tubes. A group of these samples was used for X-ray diffraction, performed in a Rigaku 300 X-ray diffractometer using Cu K_α X-ray at 60 kV and 300 mA. A second group of samples was studied in the superconducting quantum-interference device (SQUID) to determine the thermodynamic-equilibrium value of magnetization at room temperature. Finally, the third group of samples was prepared for observation in the transmission electron microscope. The samples were polished and the central portion of the rectangles thinned to electron transparency in a jet-polishing apparatus. The electrolyte used was 590 mL methanol, 350 mL m-butanol, and 60 mL perchloric acid, and the thinning procedure was performed at −10 °C at a voltage of 25 to 30 V and a current of 0.10 to 0.15 A.

III. RESULTS

A. *Transmission Electron Microscopy Observations*

The sample deformed at 10^{-3} s^{-1} exhibits extensive slip deformation (Figure 2), the presence of stacking faults (Figure 3), and the formation of α'-martensite (Figure 4). On the other hand, the sample deformed at high velocities and up to 5 pct strain exhibits extensive stacking-fault formation (Figure 5) and the presence of microtwins laying on the (111) closed-packed planes (Figure 6). Additional deformation, up to 25 pct strain at high velocities, caused the appearance of a second twin variant on a related (111)-type plane, with an orientation of 109 deg with respect to the primary variant (Figure 7). Furthermore, high-velocity deformation up to 25 pct strain induced the formation of ε-martensite (Figure 8), whereas the formation of α'-martensite was suppressed.
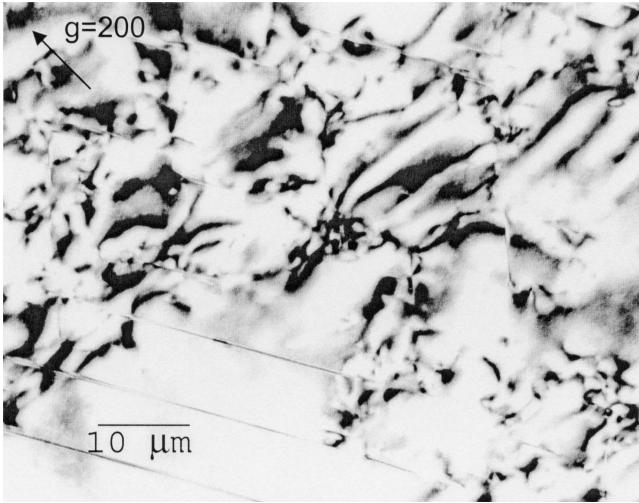
Fig. 2—Slip deformation during deformation at low strain rates. The total strain is 25 pct. Beam direction, $B = [011]$.
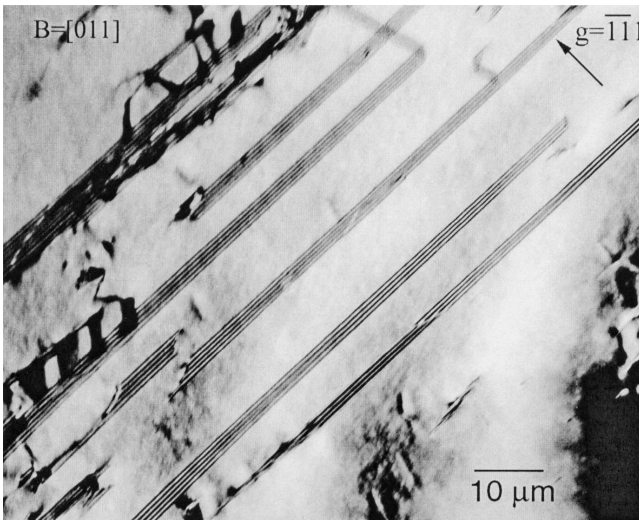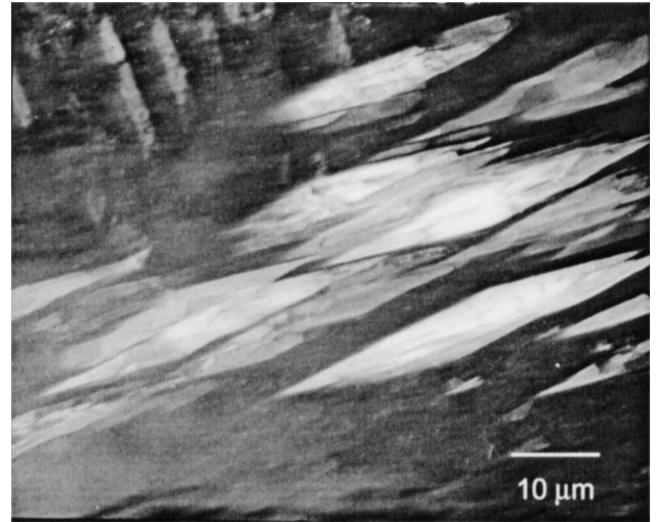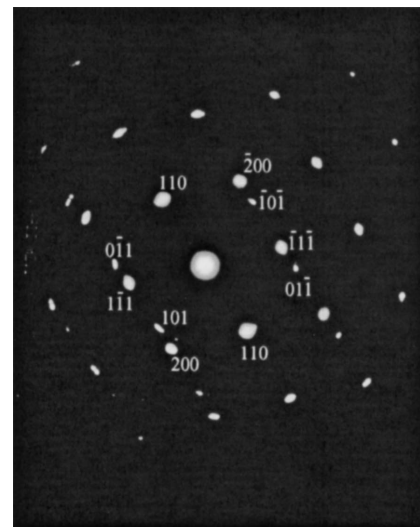

Fig. 3—Stacking-fault formation during deformation at low strain rates. The total strain is 25 pct. Beam direction, $B = [011]$.

(a)

(b)

Fig. 4—Formation of α'-lath martensite during deformation at low strain rates. The total strain is 25 pct. (a) Dark-field image. (b) Selected-area diffraction pattern taken with the beam direction, $B = [011]_\gamma // B = [\bar{1}11]_\alpha'$.

B. X-Ray Diffraction

The X-ray diffraction analysis corresponding to the undeformed material is shown in Figure 9(a). As expected, the sample exhibits the presence of mainly γ-austenite phase and some amount of δ-ferrite. After 25 pct strain at low strain rates, the amount of α'-martensite has increased, as is evident from Figure 9(b) ((110) α'-peak at about $2\theta = 44$ deg). For samples deformed at high strain rates and 5 pct strain, there is some formation of α'-martensite with respect to the undeformed sample (Figure 9(c)), but much less than for the low-strain-rate case. For samples deformed at high strain rates and 25 pct strain, the suppression of α'-martensite is slightly higher than for samples deformed at high strain rates and 5 pct strain. Moreover, additional peaks appeared in the X-ray spectrum at approximately $2\theta = 47$ and 61 deg (Figure 9(d)), which have been assigned to the hexagonal ε-martensite phase. In
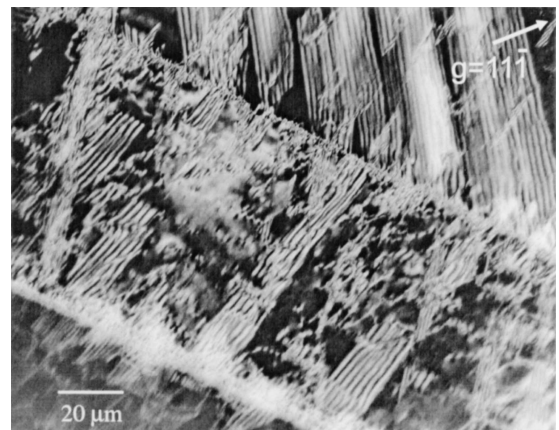

Fig. 5—Extensive stacking-fault formation during deformation at high strain rates and 5 pct strain. The majority of the stacking faults are nucleated at grain boundaries. Beam direction, $B = [011]$.
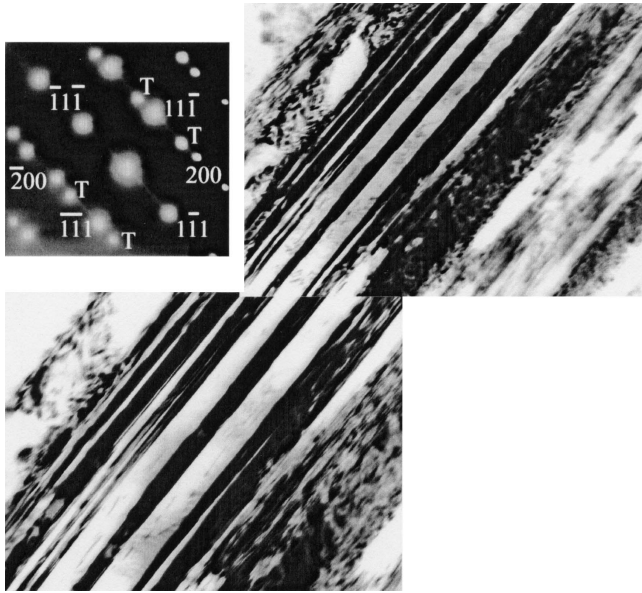
Fig. 6—Formation of microtwins during deformation at high strain rates and 5 pct strain. Twinning becomes the main mode of deformation at high strain rates. The spots in the diffraction pattern labeled "T" are twin spots. Beam direction, B = [011].
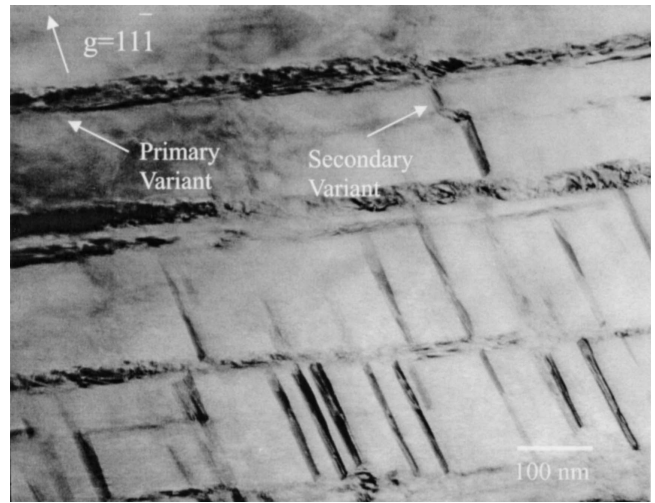

Fig. 7—Formation of a second twin variant during deformation at high strain rates and 25 pct strain. The second variant seems to be nucleated on the primary twin variant. Beam direction, B = [011].
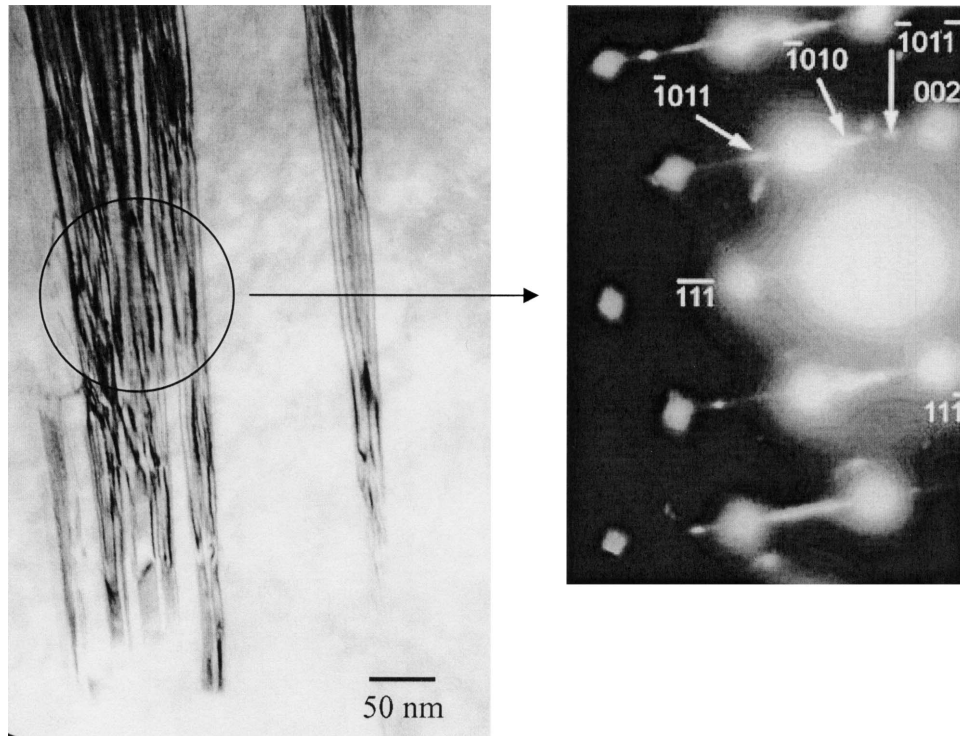

Fig. 8—Formation of hcp ε-martensite during high velocity deformation and 25 pct strain. The diffraction pattern obtained from the region limited by the solid circle shows the presence of extra spots, which correspond to the hcp-martensite phase. The beam direction, $B = [1\bar{1}0]_{\text{fcc}}//[1\bar{2}10]_{\text{hcp}}$.

Figure 10, the ratios of austenite to δ-ferrite and of austenite to α'-martensite, associated with the undeformed and deformed samples, respectively, are presented. The ratio of austenite to δ-ferrite was determined by the X-ray intensity ratio $\{200\}\gamma/\{110\}\delta$, whereas the ratios of austenite to α'-martensite were determined from the X-ray intensity ratio $\{200\}\gamma/\{110\}\alpha'$.

The reason for choosing these peaks and not the $\{111\}\gamma/\{110\}\delta$ or the $\{111\}\gamma/\{110\}\alpha'$ is due to the fact that the $\{0002\}$ planes of the hcp martensite are parallel to the $\{111\}$ planes of the austenite and, thus, would contribute to the $\{111\}\gamma$ peak. As shown in Figure 10, for the same amount of strain (25 pct), deformation at high velocities reverses the tendency
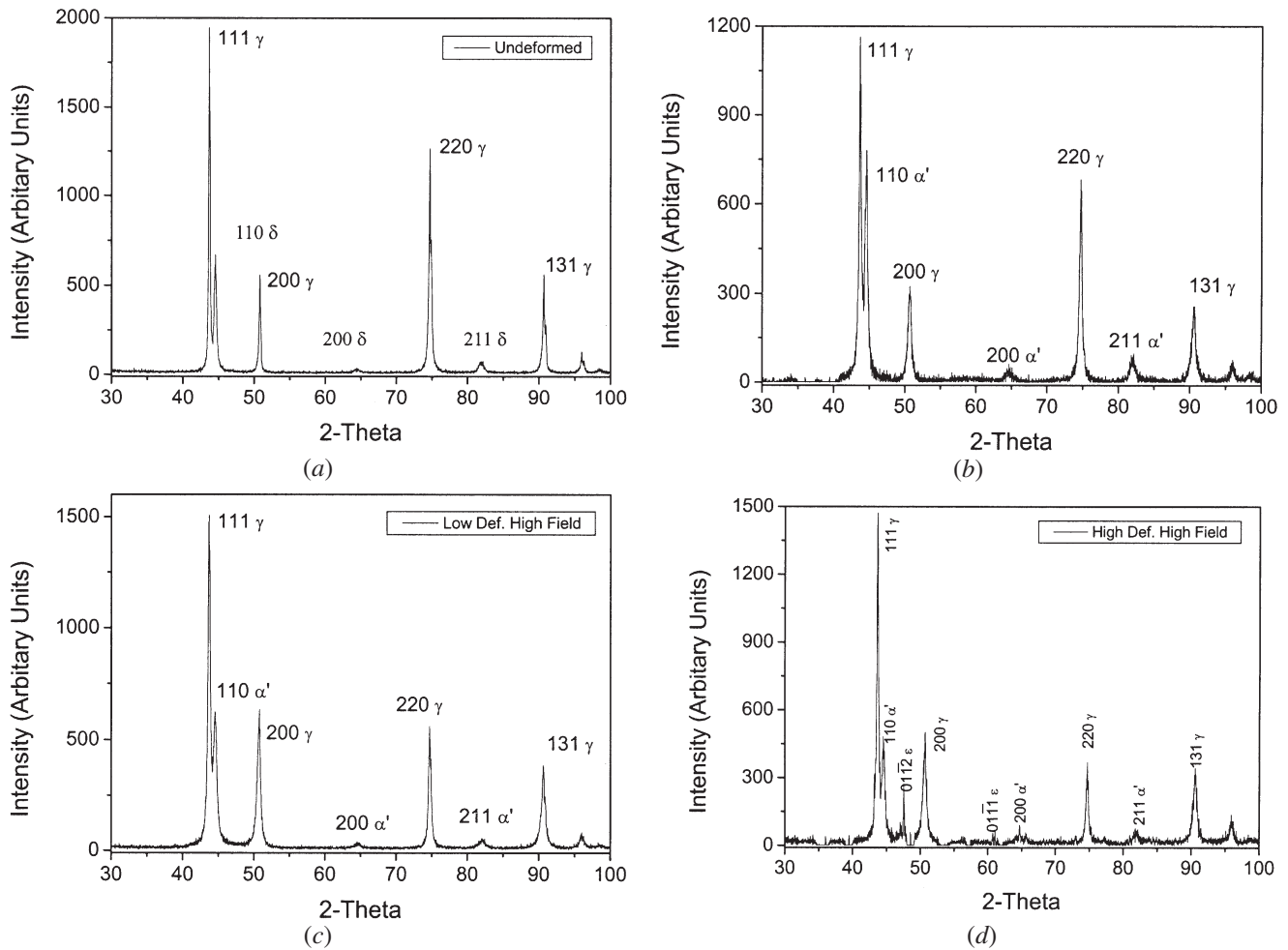
Fig. 9—X-ray diffraction spectra for the undeformed sample and the specimens deformed under various conditions: (*a*) undeformed, (*b*) low strain rate and 25 pct strain, (*c*) high strain rate and 5 pct strain, and (*d*) high strain rate and 25 pct strain.
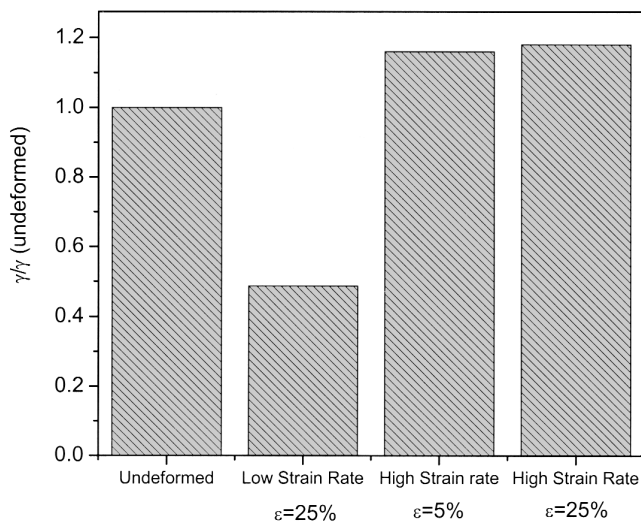

Fig. 10—Amount of austenite normalized with respect to the austenite content in the undeformed sample as a function of the various deformation conditions. The austenite to δ-ferrite ratio in the underformed sample was determined by the X-ray intensity ratio $\{200\}\gamma/\{110\}\delta$, whereas the austenite to α'-martensite ratio in the deformed samples was determined from the X-ray intensity ratio $\{200\}\gamma/\{110\}\alpha'$. Note the significant decrease of the amount of austenite for the case where the sample was deformed at low strain rates. On the other hand, high-strain-rate deformation increases significantly the amount of austenite.

of stress-induced α'-martensite formation and leads to enhanced austenite stability.

C. *The SQUID Analysis*

The intrinsic magnetic properties of the alloys deformed at low and high strain rates are shown in Figure 11 in the form of *M-H* curves. For the samples deformed at low strain rates (25 pct strain), the saturation magnetization is $M_s = 87$ emu/cm^3, and technical saturation is achieved for 2.7 kOe. For the samples deformed at high strain rates and 25 pct strain, $M_s = 20$ emu/cm^3, and saturation occurs for $H = 1.2$ kOe. In both cases, the coercive force is $H_c = 130$ Oe. The higher saturation magnetization exhibited by the alloy deformed at low strain rates is an indication of a higher amount of ferromagnetic phase, *i.e.*, α'-martensite.

IV. DISCUSSION

Despite the fact that only two strain rates and two levels of strain have been tested, the transmission electron microscopy (TEM) observations and X-ray analysis enable us to construct a schematic diagram in which the various structures can be depicted as a function of strain rate and level of strain
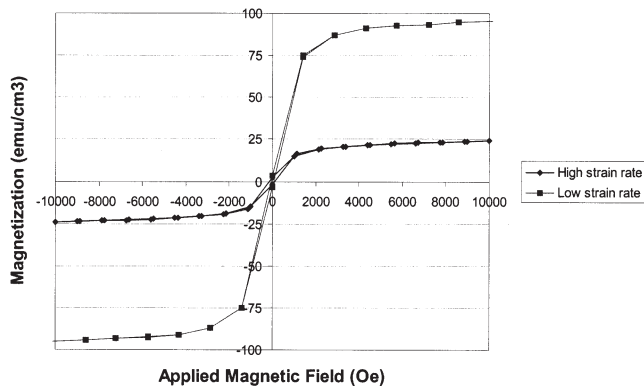
Fig. 11—Magnetic hysteresis loop for samples deformed at low and high strain rates and 25 pct strain. The large difference in magnetization indicates that the sample deformed at low strain rates contains a significantly larger amount of ferromagnetic α-martensite.
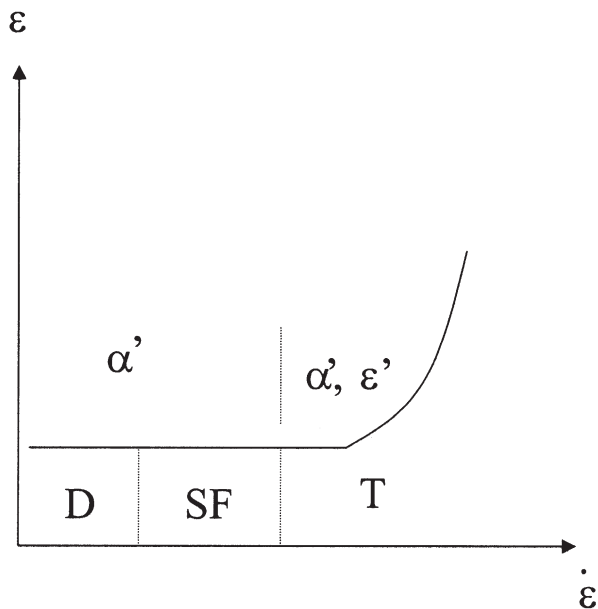

Fig. 12—Strain *vs* strain rate diagram tentatively showing the regions where the various phases are likely to exist: D = dislocations, SF = stacking faults, T = twins, α' = bct martensite, and ε' = hcp martensite.

(Figure 12). One important aspect that arises from the observation of Figure 12 is the sequence dislocations (D) $\rightarrow$ stacking faults (SF) $\rightarrow$ Twins (T), which is driven by increasing the deformation rate. As the strain rate increases, the ratio of perfect dislocations to partial dislocations decreases, whereas at very high strain rates, twinning becomes the main mode of deformation. This sequence of events can be discussed in terms of nucleation of defects and dislocation motion.

A. *Nucleation of Defects*

Assuming the same nucleation mechanism for all the deformation modes, we discuss the homogeneous nucleation of both a perfect dislocation loop and a partial dislocation

loop. For the perfect dislocation loop, the energy required to nucleate a loop of radius R can be expressed as[12]

$$\Delta G^{\text{perfect}} \cong -\pi R^2 \sigma \mathbf{b}_0 + \frac{1}{2} \mu \mathbf{b}_0^2 R \ln \left(\frac{4R}{r} \right) \quad [1a]$$

where σ is the shear stress acting on the plane of the loop, μ is the shear modulus, $\mathbf{b}_0$ is the Burgers vector of the perfect dislocation, and r is the core radius of the dislocation loop. The condition for a loop of critical size, $\partial \Delta G/\partial R = 0$, then gives

$$R_C^{\text{perfect}} \cong \left(\frac{\mu \mathbf{b}_0}{4\pi\sigma} \right) \left(\ln \left(4R_C/r \right) + 1 \right) \quad [1b]$$

For a partial dislocation loop, Eq. [1] needs to be altered, as the nucleation of an imperfect dislocation loop will involve the formation of a stacking fault. Thus, for an intrinsic stacking-fault loop, we can write

$$\Delta G^{\text{partial}} \cong -\pi R^2 \sigma \mathbf{b}_P + \frac{1}{2} \mu \mathbf{b}_P^2 R \ln \left(\frac{4R}{r} \right) + \pi R^2 \gamma \quad [2a]$$

where $\mathbf{b}_P$ is the Burgers vector of the partial dislocation, γ is the SFE, and the other symbols retain the same meaning as in Eq. [1a]. Following the previous procedure, the determination of the critical-size loop yields

$$R_C^{\text{partial}} \cong \left(\frac{\mu \mathbf{b}}{4\pi(\sigma - \gamma/\mathbf{b}_P)} \right) \left(\ln \left(4R_C/r \right) + 1 \right) \quad [2b]$$

Equations [1] and [2] show that for a perfect dislocation loop, the activation-energy barrier for nucleation will depend on the level of stress and the Burger's vector, whereas, for a partial dislocation loop, the activation-energy barrier for nucleation will depend on the SFE, in addition to σ and $\mathbf{b}_P$. Assuming the Burgers vector of a perfect dislocation, $\mathbf{b}_0 = a/2 <110> = 2.53 \times 10^{-10}$ m,[13] where a is the lattice parameter of the austenite phase, the Burgers vector of a partial dislocation is $\mathbf{b}_P = a/6 <112> = 1.46 \times 10^{-10}$ m,[13] and the SFE is $\gamma = 0.020$ J/m^2,[14] we can plot the activation energy of nucleation (ΔG) for a perfect and for a partial dislocation loop, as a function of the loop radius. For the calculations, we will use a range of shear stresses from $\sigma = 1$ GPa to $\sigma = 160$ MPa. This is shown in Figure 13, where the activation-energy barrier required for nucleation is represented by the maximum of the free-energy function. Observation of Figure 13 shows that for shear stresses of 1 GPa and 300 MPa (Figures 13(a) and (b)), the nucleation of a partial loop is favored with respect to a perfect loop. This is supported by the fact that for shear stresses of 300 MPa and 1 GPa, the maximum of the energy function is lower for the partial loop than for the perfect loop. However, for a shear stress of 160 MPa, the perfect loop is easier to nucleate than the partial loop. This is shown in Figure 13(c), for which the energy maximum for a perfect loop is found at approximately $R = 800$ Å, whereas for the partial loop, the energy function continues to increase beyond the 800 Å loop radius, assuming higher-energy values than that of a perfect loop before reaching a maximum.
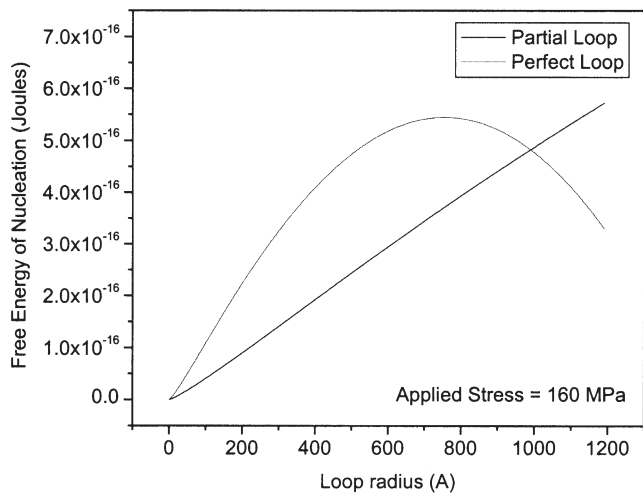
In general, one can determine the critical value of the shear stress, for which the nucleation of partial dislocation loops is favored with respect to the nucleation of perfect loops. This can
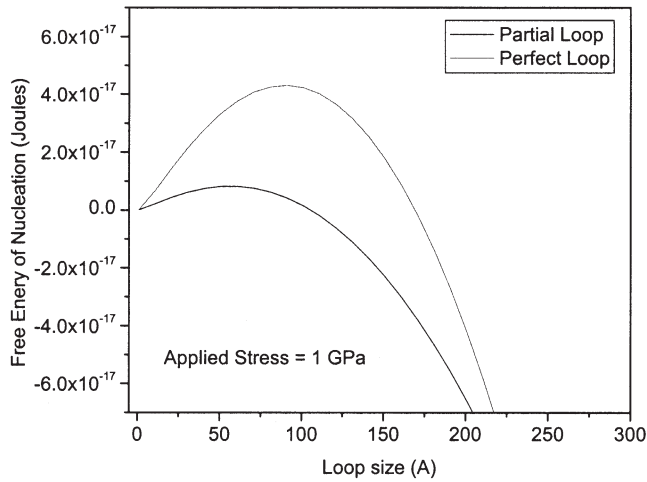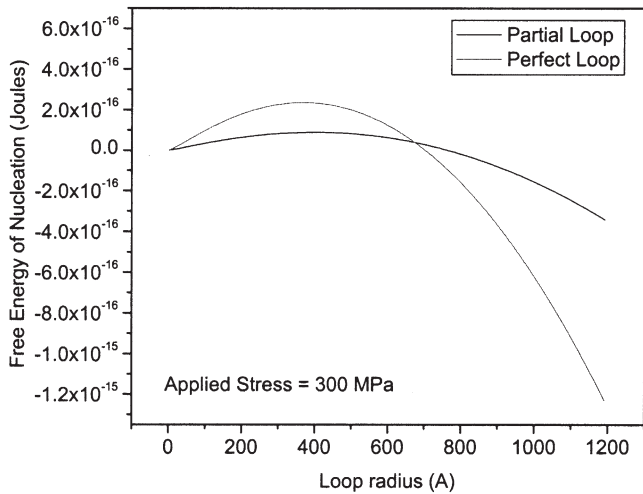
Fig. 13—Activation energy of nucleation for a perfect and a partial dislocation loop, as a function of the loop radius for three different regimes of shear stresses: (a) $\sigma = 1$ GPa, (b) $\sigma = 300$ MPa, and (c) $\sigma = 160$ MPa.

be calculated by equating the critical Gibbs free energies for nucleation of a perfect loop and a partial loop, in the form

$$\Delta G_C^{\text{perfect}} = \Delta G_C^{\text{partial}} \qquad [3]$$

On the basis of Eqs. [1a] and [1b], we can write, for the critical free energy of nucleation of a perfect dislocation loop, the expression

$$\Delta G_C^{\text{perfect}} = \frac{\mu^2 \mathbf{b}_0^3}{16\pi\sigma} (A^2 - 1) \qquad [4a]$$

where $A = \ln (R_C^{\text{perfect}}/r)$, and, on the basis of Eqs. [2a] and [2b], we can write, for the critical free energy of nucleation of a partial dislocation loop, the expression

$$\Delta G_C^{\text{partial}} = \frac{\mu^2 \mathbf{b}_P^3}{16\pi\left(\sigma - \dfrac{\gamma}{\mathbf{b}_P}\right)} (B^2 - 1) \qquad [4b]$$

where $B = \ln (R_C^{\text{partial}}/r)$. Thus, from Eq. [3], we find

$$\frac{\gamma}{\sigma} = \mathbf{b}_P \left(1 - \frac{\mathbf{b}_P^3 (B^2 - 1)}{\mathbf{b}_0^3 (A^2 - 1)} \right). \qquad [5]$$

Using the values for the SFE and the Burgers vectors of the perfect and partial dislocations mentioned previously, a simple calculation shows that the critical shear-stress value required to enhance the nucleation of partial dislocation loops in 304 stainless steel is approximately $\sigma_C = 184$ MPa. Hence, at higher shear stresses, the nucleation of partial dislocations is more likely to occur than the nucleation of perfect dislocations.

On this basis, we can argue that at fast strain rates, all the deformation occurs in extremely short times and, thus, higher kinetic energies imposed during the impact lead to higher levels of applied stress, which enhance stacking-fault nucleation. In addition, the barrier for nucleation can be more easily overcome in regions of stress concentration. Preferred nucleation in these locations is, therefore, expected, an example of which is shown in Figure 5.

For the case of three-layer twins, we shall assume that the nucleation occurs by the mechanism where partial dislocations are emitted on successive closed-packed planes. Thus, as the shear stress is increased, more partial dislocations are nucleated, and, thus, it becomes highly probable to have partial dislocations on every plane. As a result, from a nucleation point of view, twin structures become the most favorable defects at the highest strain rates.

B. Dislocation Motion

In the previous section, we have discussed the effect of strain rate on the nucleation of dislocations. However, prior to the deformation tests, the material possesses a number of dislocations that will try to move to accommodate the strains imposed by deformation. Because of the short deformation times involved at high strain rates, we shall argue that in some cases dislocation motion is not readily activated. Although this is still not fully understood, we suggest that at high strain rates, perfect dislocations do not have time to respond to the applied stress due to their lower jump frequency. An argument to support this view is presented as follows.

Let us assume that dislocation motion is controlled by kink nucleation and mobility. We assume this mechanism to be important for the onset of dislocation motion, but not for high-velocity "cruise" motion when phonon drag effects may dominate. In addition, we neglect the SFE term in the equations of kink nucleation, which might have a small contribution.

Assuming a dislocation of finite length, such that kink pairs of height a and length w (w is assumed to be much smaller than the dislocation length) can nucleate and move parallel to the dislocation line, the velocity of the dislocation normal to itself can be written as[12]

$$V_k = a\lambda J$$

where λ, the average distance between kink pairs, is the distance along the dislocation line that the kink pair needs to move before merging into the adjacent kink pair, and J is the nucleation rate of kink pairs per unit length of dislocation line per unit time. This nucleation rate, under the presence of a shear stress of σ, can be expressed as

$$J = \frac{f_f}{w + \lambda} \exp\left(\frac{-2W_k + \sigma\mathbf{b}^3}{kT}\right) \quad [6]$$

where f_f is the attempt frequency for a jump, assumed to be approximately equal to the Debye frequency; w is the length of the kink pair; λ is the distance between kink pairs; and W_k is the energy of formation of a single kink of length a, given by[12]

$$W_k = \frac{2a}{\pi}\left(2W_p W_0\right)^{1/2} \quad [7]$$

for which the Peierls energy per unit length of kink (W_p) is given by[12]

$$W_p = \frac{\mu\mathbf{b}^2}{\pi(1 - v)} \exp\left(-\frac{4\pi\xi}{\mathbf{b}}\right) \quad [8]$$

and the line energy per unit length of kink (W_0) is given approximately by[12]

$$W_0 = \frac{\mu\mathbf{b}^2}{4\pi(1 - v)}\left((1 + v)\cos^2\beta + (1 - 2v)\sin^2\beta\right)\ln\frac{R}{r} \quad [9]$$

where k is Boltzman's constant; T is the temperature; μ is the shear modulus; $\mathbf{b}$ is the Burgers vector; v is the Poisson's ratio; ξ is the half-width of the dislocation and is typically assumed to be $\xi = d/2$, where d is the interplanar spacing; β is the angle between the Burgers vector and the dislocation line direction; and r is the cut-off parameter.

Thus, the frequency (f_k) by which a dislocation advances a Burgers vector due to the nucleation and lateral motion of kink pairs is given by
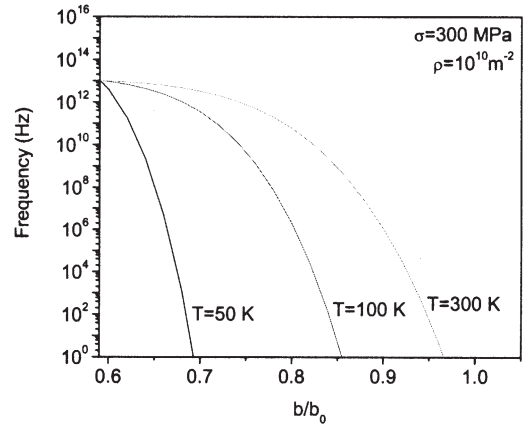
$$f_k = \frac{V_k}{\mathbf{b}} = \frac{a\lambda J}{\mathbf{b}} = \frac{a\lambda}{\mathbf{b}(w + \lambda)} f_f \exp\left(\frac{-2W_k + \sigma\mathbf{b}^3}{kT}\right) \quad [10]$$

Assuming $a \approx \mathbf{b}$, consider the two cases $w \ll \lambda$ or $w \approx \lambda$. On these assumptions, we can rewrite Eq. [10] as
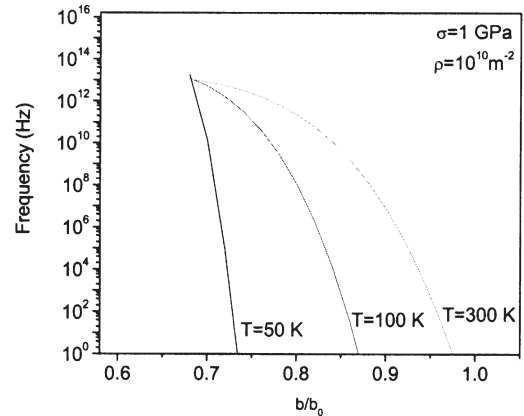
$$f_k = Cf_f \exp\left(\frac{-2W_k + \sigma\mathbf{b}^3}{kT}\right) \quad [11]$$
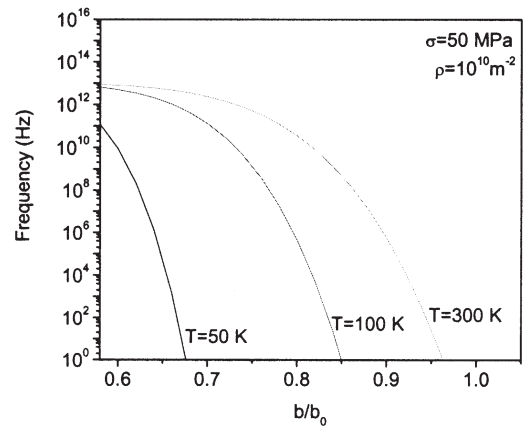
(a)

(b)

(c)

Fig. 14—Dependence of frequency f_k on the Burgers vector, normalized with respect to the Burgers vector of a perfect dislocation ($\mathbf{b}_0$) for different temperatures and stress levels: (a) 50 MPa, (b) 300 MPa, and (c) 1 GPa. The points where the three curves intersect correspond to a critical Burgers vector, below which the rate at which dislocations advance a Burgers vector due to the nucleation and lateral motion of kinks is temperature independent.

where $C = 1$ for $w \ll \lambda$ and $C = 1/2$ for $w \approx \lambda$. Assuming $C = 1$, $W_0 = W_p/10^{-3}$,[12] $a \approx b = 2.53$ Å for a perfect dislocation and 1.46 Å for a partial dislocation,[13] $k = 1.38 \times 10^{-23}$ N·m/K, $T = 300$ K, $\mu = 7.31 \times 10^{10}$ N/m²,[13] $v = 0.33$,[13] $d = 1.035$ Å, $f_f = 1 \times 10^{13}\text{s}^{-1}$,[12] and $w \ll \lambda$, we can plot f_k as a function of the Burgers vector for different temperatures and levels of stress (Figure 14). As shown in

Figure 14, there is a very strong dependence of the rate of kink-pair formation on the dislocation Burgers vector. In addition, for each level of stress, there is a value $\mathbf{b}/\mathbf{b}_0$ at which the relation between f_k and the dislocation Burgers vector is temperature independent (for example, $\mathbf{b}/\mathbf{b}_0 = 0.7$ for $\sigma = 1$ GPa). This value is the threshold value below which the nucleation and lateral motion of kinks is not thermally activated.

In order to understand the effect of high velocity on the mechanism of dislocation motion, we now compare, for a particular shear stress, the frequency (f_k) by which a dislocation moves due to the nucleation and motion of kink pairs with the frequency (f_d) by which a dislocation advances a Burgers vector, in order to match the inferred strain rate. The frequency f_d can be written as

$$f_d = \frac{V_d}{\mathbf{b}}$$ [12]

where V_d is the average velocity at which dislocations must move, and $\mathbf{b}$ is the Burgers vector. The average velocity of moving dislocations can be related to the strain rate ($\dot{\varepsilon}$) by

$$\dot{\varepsilon} = \rho \mathbf{b} V_d$$ [13]

where ρ is the mobile dislocation density, and the other symbols have the same meaning as before. Hence, we can rewrite Eq. [12] in the form

$$f_d = \frac{\dot{\varepsilon}}{\rho \mathbf{b}^2}$$ [14]

Figure 15 shows a plot of f_d as a function of the Burgers vector (Eq. [12]) for different dislocation densities and strain rates. The decrease of f_d for larger Burgers vectors is evident, although the correlation seen is much less pronounced than the dependence of the kink nucleation rate on the Burgers vector, shown in Figure 14.

In this context, we should define a critical frequency required to move a dislocation at a velocity of V due to the nucleation and lateral motion of kink pairs. This occurs for

$$f_k > f_d$$ [15]

A comparison of both f_k and f_d as a function of the Burgers vector for various temperatures and strain rates is shown in Figure 16. The points where the two frequencies are equal correspond to the critical Burgers vector, above which dislocations do not respond to the imposed strain rate. As shown in Figure 16, for high strain rates and low temperatures, mobile dislocations tend to have smaller Burgers vectors, for which f_k is greater than the frequency f_d imposed by deformation. As a result, one may argue that partial dislocations tend to be more operative under low temperatures and high strain rates, which can then lead to the formation of twins. Although this trend is quite clear from the observation of Figure 16, we should mention that the calculations are very sensitive to the dislocation width and are relatively dependent on the exact values of shear stress, which were not available to us. These aspects can explain the fact that, according to Figures 14 through 16, perfect dislocations could not accommodate the imposed strain rate for the experimental conditions performed. However, the model developed herein clearly shows semiquantitative trends only.

The behavior at high strain rates and room temperature is then equivalent to the behavior at low temperatures and low
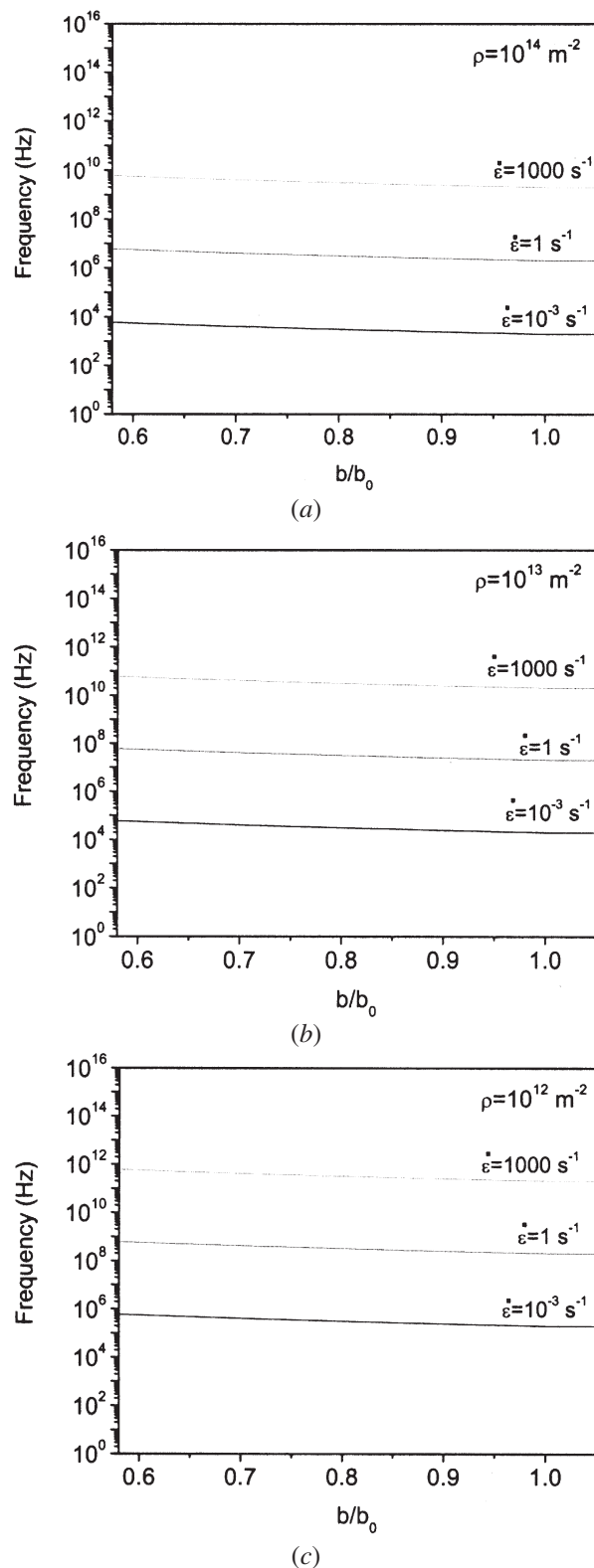

Fig. 15—Dependence of frequency f_d on the Burgers vector, normalized with respect to the Burgers vector of a perfect dislocation ($\mathbf{b}_0$) for different strain rates and dislocation densities: (a) $\rho = 10^{14}$ m^{-2}, (b) $\rho = 10^{13}$ m^{-2}, and (c) $\rho = 10^{12}$ m^{-2}.

strain rates, for which twinning is the principal mode of deformation. In this case, under an applied stress, perfect dislocation motion is not easily accomplished due to lower kink nucleation
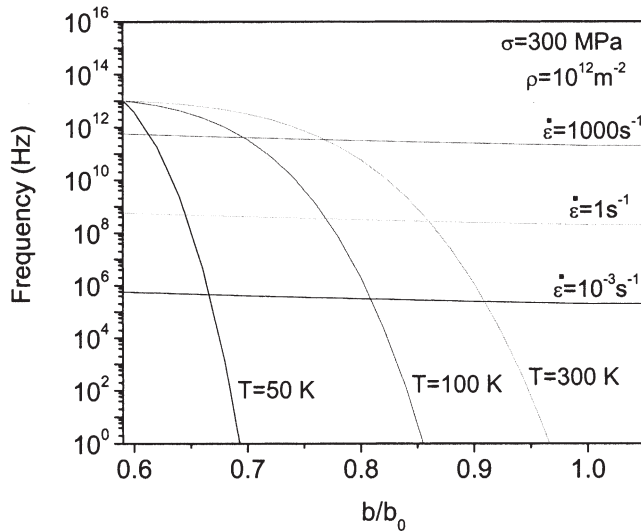
(a)
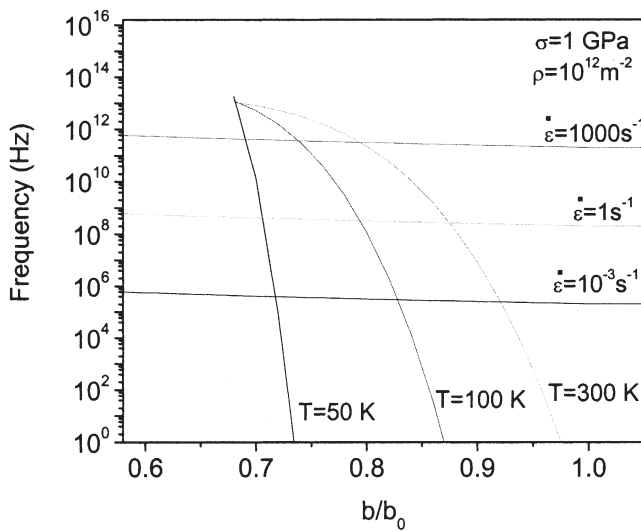
(b)

Fig. 16—Comparison between the frequency f_k and the frequency f_d at various strain rates as a function of the normalized Burgers vector $\mathbf{b}/\mathbf{b}_0$, for different temperatures and two levels of stress: (a) 300 MPa and (b) 1 GPa. The dislocation density is 10^{12} m^{-2}, which is typical of annealed metals.

rates and, thus, the imposed strain can be more readily accommodated by partial dislocation motion.

In addition to the aforementioned mechanisms, the behavior of dislocations at high strain rates and low temperatures also suggests that microstructures with a high density of pre-existing perfect dislocations will inhibit the formation of microtwins. This is due to the fact that pre-existing perfect dislocations may be able to move under stress and release some of the strain, thus affecting the microtwin nucleation process. Moreover, pre-existent perfect dislocations will interact with propagating microtwins, leading to a reduction of the mobile twin density.

C. Influence of Adiabatic Heating and Phase Transformations

As shown in Figures 4 and 9 through 12, α'-martensite is more prone to appear at large strains and low strain rates. For large strains, an increase in the strain rate induces the
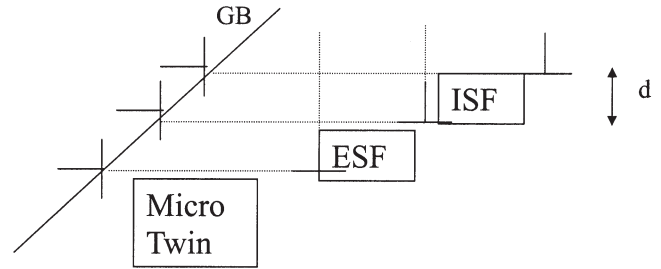

Fig. 17—Formation of a microtwin by emission of three partial dislocations from a grain boundary. GB = grain boundary, ISF = intrinsic stacking fault, and ESF = extrinsic stacking fault.

formation of ε-martensite (Figures 8 and 9). However, as the strain rate is increased, more strain is required to promote the formation of the martensite phases. Thus, for very high strain rates, twinning becomes the principal mode of deformation, as shown in Figures 7, 8, and 12.

The reasons for the enhanced suppression of α'-martensite during high-strain-rate deformation lies in the fact that there is adiabatic heating during high-velocity deformation processes. The temperature rise in the specimen due to conversion of plastic work into heat is given by[3]

$$\Delta T = \frac{\psi}{d_\rho \, C_p} \int \sigma(\varepsilon) d\varepsilon \qquad [16]$$

where d_ρ is the density, C_p is the specific heat, and ψ is the fraction of work converted into heat, which is assumed to be approximately 1. Assuming a value of $d_\rho/C_p = 3.60$ MPa/K,[3] $\int \sigma(\varepsilon) d\varepsilon = 180$ MPa for a deformation of $\varepsilon = 0.20$ and a strain rate of $\dot{\varepsilon} = 100$ s^{-1} and $\int \sigma(\varepsilon) d\varepsilon = 221$ MPa for a deformation of $\varepsilon = 0.20$ and a strain rate of $\dot{\varepsilon} = 5000$ s^{-1}; the estimated temperature increase in the sample can be anywhere between 50 and 62 K. Coupling this information with the knowledge that the strain rate used in this work is close to 1000 s^{-1}, leads us to expect that a change in temperature, greater than 50 K, may be sufficient to stabilize the austenite phase and suppress the martensite phase.

Although higher strain rates decrease the presence of the α'-martensite phase, high-velocity deformation promotes the formation of the ε-martensite hcp phase (Figures 8, 9, and 12). The principal difference between the formation of a microtwin and an embryo of hcp phase is the number of planes separating the emission of partial dislocations. In the case of a microtwin, partial dislocations need to be activated on every consecutive plane (Figure 17), whereas for the hcp martensite, partial dislocations are necessary on every other close-packed plane (Figure 18). This similarity is an indication that the basic unit involved in the formation of either structure is a partial dislocation of type $a/6\langle 112 \rangle$. As the stress is increased, more partial dislocations are nucleated and emitted, and, thus, it becomes more probable to have partial dislocations on every plane or every other plane. Of these two options, twinning is the most favorable, as no stacking faults are present and, thus, lattice distortions perpendicular to the stacking fault do not contribute to the total strain energy.[15]

The superplastic behavior encountered in samples which have been deformed at high strain rates[1,2] is worth examining. Hu et al.[16,17] have suggested that as a result of deformation at high strain rates, inertial effects can diffuse neck growth,
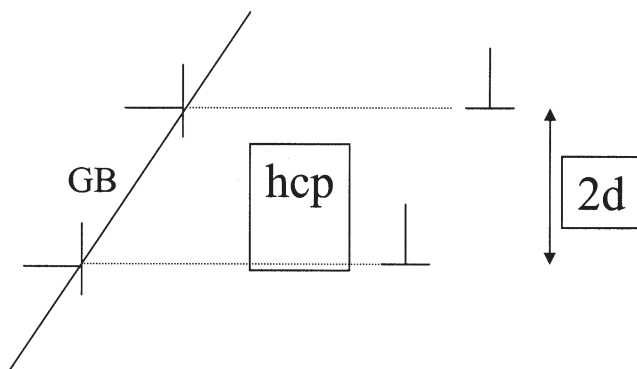
Fig. 18—Formation of a hcp martensite embryo by emission of partial dislocations on every other close-packed plane.

high velocity can cause the material to spread laterally in a plastic fashion, and the material's constitutive behavior can be changed. In addition to these claims, we argue that at the microstructural level, dislocation velocity will also play an important role. At high strain rates, dislocation velocity is such that it does not allow enough time for dislocations to reorganize into stable configurations that are rate controlling for velocities lower than 0.1 pct of the transverse sound-wave velocity. As a result, plastic deformation can proceed readily and, thus, hardening will be hindered. This suggests that predeforming the material prior to high-velocity deformation would enhance the interaction between dislocations and, thus, one would expect a greater hardening rate.

V. CONCLUSIONS

From this work on high-strain-rate deformation of an austenitic stainless steel, we can draw the following conclusions.

1. High strain rates successively induce the formation of stacking faults and twin structures. At the highest strain rates, the number of twin variants increases from one to two variants, whose habit planes are related variants of the type $(1\bar{1}1)$ and $(11\bar{1})$.
2. The sequential tendency for the presence of perfect dislocations, stacking faults, and twin structures as the strain rate increases can be explained in terms of easy nucleation of partial dislocations at high strain rates and of the enhanced ability of partial dislocations to respond to higher strain rates due to their higher jump frequency.
3. The formation of α'-martensite is suppressed by increasing the strain rate during electromagnetic deformation due to the adiabatic heating generated during the high-velocity deformation processes.
4. The tendency for ε-martensite formation increases with increasing strain rates.

REFERENCES

1. V.S. Balanethiram and G.S. Daehn: *Scripta Metall.*, 1992, vol. 27, pp. 1783-88.
2. V.S. Balanethiram and G.S. Daehn: *Scripta Metall.*, 1994, vol. 30, pp. 515-20.
3. P.S. Follansbee: in *Metallurgical Applications of Shock-Wave and High-Strain-Rate Phenomena*, L.E. Murr, K.P. Staudhammer, and M.A. Meyers, eds., Marcel Dekker, Inc., New York, NY, 1986, pp. 451-79.
4. M.A. Meyers and L.E. Murr: *Proc. Int. Conf. on Metallurgical Effects of High-Strain-Rate, Deformation and Fabrication*, M.A. Meyers and L.E. Murr, eds., Plenum Press, New York, NY, 1980, pp. 487-530.
5. L.E. Murr: *Proc. Int. Conf. on Metallurgical Effects of High-Strain-Rate, Deformation and Fabrication*, M.A. Meyers and L.E. Murr, eds., Plenum Press, New York, NY, 1980, pp. 607-73.
6. J.W. Christian and S. Majahan: *Progr. Mater. Sci.*, 1995, vol. 39, pp. 1-157.
7. V. Caballero and S.K. Varma: *J. Mater. Sci.*, 1999, vol. 34, pp. 461-68.
8. G.T. Gray III and J.C. Huang: *Mater. Sci. Eng.*, 1991, vol. A145, pp. 21-35.
9. K.P. Staudhammer, C.E. Frantz, S.S. Hecker, and L.E. Murr: *Proc. Int. Conf. on Metallurgical Effects of High-Strain-Rate, Deformation and Fabrication*, M.A. Meyers and L.E. Murr, eds., Plenum Press, New York, NY, 1980, pp. 91-112.
10. K.A. Johnson and K.P. Staudhammer: in *Metallurgical Applications of Shock-Wave and High-Strain-Rate Phenomena*, L.E. Murr, K.P. Staudhammer, and M.A. Meyers, eds., Marcel Dekker, Inc., New York, NY, 1986, pp. 525-42.
11. L.E. Murr: *Proc. Int. Conf. on Metallurgical Effects of High-Strain-Rate, Deformation and Fabrication*, M.A. Meyers and L.E. Murr, eds., Plenum Press, New York, NY, 1980, pp. 753-77.
12. J.P. Hirth and J. Loethe: *Theory of Dislocations*, Wiley Interscience, New York, NY, 1982.
13. H.M. Ledbetter: *Met. Sci.*, 1980, vol. 14, pp. 595-96.
14. P.J. Ferreira and P. Mullner: *Acta Mater.*, 1996, vol. 46, pp. 4479-84.
15. P. Müllner and P.J. Ferreira: *Phil. Mag. Lett.*, 1996, vol. 73, pp. 289-97.
16. X. Hu and G.S. Daehn: *Acta Metall., Acta Mater.*, 1996, vol. 44, pp. 1021-33.
17. M. Altynova, X.Y. Hu, and G.S. Daehn: *Metall. Mater. Trans. A*, 1996 vol. 27A, pp. 1837-44.